Comparison of laser-based mitigation of fused silica surface damage using mid- versus far-infrared lasers

S. T. Yang, M. J. Matthews, S. Elhadj, D. Cooke,
G. M. Guss, V. G. Draggoo, P. J. Wegner

February 16, 2010

Applied Optic

Comparison of laser-based mitigation of fused silica surface damage using mid- versus far-infrared lasers

Steven T. Yang,[*] Manyalibo J. Matthews, Selim Elhadj, Diane Cooke, Gabriel M. Guss, Vaughn G. Draggoo, and Paul J. Wegner

Lawrence Livermore National Laboratory, 7000 East Ave., Livermore CA, USA

[*] *Corresponding author: yang9@llnl.gov*

Laser induced growth of optical damage can limit component lifetime and therefore operating costs of large-aperture fusion-class laser systems. While far-infrared (IR) lasers have been used previously to treat laser damage on fused silica optics and render it benign, little is known about the effectiveness of less-absorbing mid-IR lasers for this purpose. In this study, we quantitatively compare the effectiveness and efficiency of mid-IR (4.6 μm) versus far-IR (10.6 μm) lasers in mitigating damage growth on fused silica surfaces. The non-linear volumetric heating due to mid-IR laser absorption is analyzed by solving the heat equation numerically, taking into account the temperature-dependent absorption coefficient $\alpha(T)$ at λ=4.6 μm, while far-IR laser heating is well-described by a linear analytic approximation to the laser-driven temperature rise. In both cases, the predicted results agree well with surface temperature measurements based on infrared radiometry, as well as sub-surface fictive temperature measurements based on confocal Raman microscopy. Damage mitigation efficiency is assessed using a figure of merit (FOM) relating the crack healing depth to laser power required, under minimally-ablative conditions. Based on our FOM, we show that for cracks up to at least 500 μm in depth, mitigation with a 4.6 μm mid-IR laser is more efficient than mitigation with a 10.6 μm far-IR laser. This conclusion is corroborated by direct application of each laser system to the mitigation of pulsed laser-induced damage possessing fractures up to 225 μm in depth.

OCIS codes: 000.0000, 999.9999.

1. **Introduction**

Limiting laser-induced damages on fused silica optics is an important consideration in the design and operation of high power laser systems, such as the Mega Joule (MJ) class fusion lasers. Laser-induced damage, once initiated, has been shown to grow in diameter and depth from subsequent laser pulses, and thus can quickly compromise optical performance [1]. To arrest the growth of damage sites on fused silica optics, various mitigation techniques have been investigated [2]. At present, one of the most promising approaches is based on localized, high temperature (T > 2800 K) vaporization of damaged material using a far-infrared (IR) 10.6 μm CO_2 laser [3-6]. Surface damage sites on fused silica with diameters up to 300 μm have been successfully repaired by completely ablating away the damaged volume leaving a crater that is typically 600 μm in diameter and 30 to 40 μm deep [4]. This approach, however, tends to produce a significant amount of ablated material which can re-deposit onto the optic surface and lead to subsequent damage initiation [3]. The rim created on the edge of the ablation crater can also introduce intensification of transmitted UV light that may damage optics located down-stream[7]. Alternatively, a laser-based non-ablative approach using far-IR laser has also been demonstrated which relies on localized glass re-flow to heal damage sites at lower temperatures (T ~ 2000 K) [8]. This technique, however, is generally limited to the repair of shallow cracks (~10 μm deep) because of fuse silica's high absorption at the far-IR wavelength. It is therefore desirable to explore optical damage repair on fused silica surfaces using laser wavelengths that are less absorbing than 10.6μm, yet absorbing enough to efficiently raise surface temperatures to ~2000 K.

In terms of optical properties, fused silica is well-known for its wide and low-loss transmission window ranging from ~200nm to ~4μm (see Fig. 1). While the high transparency of silica in the visible to near infrared region is advantageous for light transmission applications, lasers operating at these wavelengths tend naturally to be ineffective for silica heating. Figure 1 shows the room temperature absorption coefficient of fused silica as a function of wavelength as reported by Kitamura *et al.* [9]. In the long-wave IR region (8~12μm), fused silica absorption is dominated by IR-active phonon bands near 9 μm, with a decreasing multiphonon absorption tail extending into the mid-IR. In the mid-IR wavelength region between 3 and 5 μm, useful for atmospheric sensing and guidance applications, fused silica absorptivity is intermediate between the peak at ~9 μm and the minimum at around 1.5 μm. In particular, the absorption length, α^{-1}, is of the same order as typical optical component thicknesses (1~100mm) over this wavelength range, as opposed to ~300nm at 9 μm. Therefore, lasers operating in the 3~5 μm mid-IR window might be expected to be more effective at heating fused silica to significant depths, and thus be more suitable for mitigating deeper sub-surface damage in silica optics.

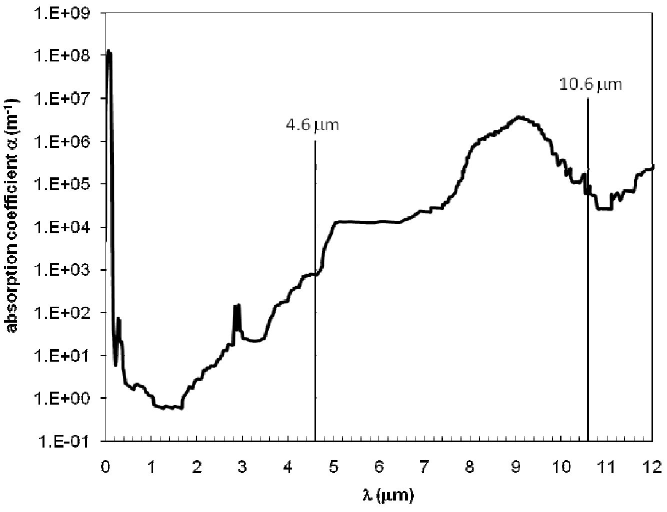

Figure 1: Room temperature absorption spectrum of fused silica reproduced from Ref. [9]. The absorption coefficient at 4.6 μm is about two orders of magnitude lower than that at 10.6 μm.

On the other hand, lasers operating in the mid-IR with >1W of continuous wave (CW) power are not as readily available as those operating at 10.6 μm. Recently, Guss *et al.* demonstrated damage mitigation on fused silica optics using a custom-built high power 4.6 μm laser [10]. In this initial demonstration, damage sites with diameters of 500 μm and crack depths of up to 200 μm were effectively mitigated with minimum surface ablation using 4.6 μm laser light that was raster-scanned over the sample using galvanometer mirrors. The resultant mitigation sites were shallow smooth pits that did not cause significant down-stream intensification of propagating UV light, and were robust to damage testing with high fluence (~25 J/cm^2) 3ns, 355 nm laser pulses. However, while this initial study clearly demonstrated the potential of using 4.6 μm lasers for localized repair of deep damage sites, the exact parameter space over which these lasers might be favored over far-IR lasers was not clear.

To more critically evaluate the use of mid-IR lasers for damage mitigation of fused silica, we present here measurements and modeling that elucidate the increased heat penetration depth, and therefore deep crack healing potential, of a 4.6 μm laser-heating as compared to that of a 10.6 μm laser-heating case. The results of our study are presented as follows: in section 2, we report, for the first time to our knowledge, quantitative high temperature measurements of $\alpha(T)$at 4.6 μm in fused silica. Based on the measured $\alpha(T)$, a numerical heat flow model of 4.6 μm laser heating is then derived. The predicted surface temperature profiles from the model are compared directly with calibrated infrared radiometry, yielding excellent agreement between modeled and measured temperature. In section 3, characterization of the heat penetration depth using measurements of the fictive temperature is presented. Using the effective crack healing depth inferred from the measured fictive temperature depth profiles, we define a damage mitigation figure of merit in section 4, and use it to quantify the difference between 4.6 μm versus 10.6 μm lasers for healing deep cracks in silica. Finally, in section 5, we illustrate the repair of laser-induced damage on fused silica surfaces using both 4.6 and 10.6μm lasers exposures and discuss the results in terms of the capillary-driven crack healing expected at high temperatures.

2. **Temperature distribution model for 4.6 and 10.6 μm laser heating**

A. Determination of the temperature-dependent absorption coefficient of fused silica at 4.6 μm

To evaluate the interaction of 4.6 μm laser radiation with fused silica which leads to a spatially-dependent temperature rise, it is important to know $\alpha(T)$ precisely over the temperature range of interest. Although α for fused silica at room temperature has been reported previously [9], no temperature-dependent data at 4.6 μm were available at the time of this study. We therefore experimentally determined $\alpha(T)$ at 4.6 μm by measuring the transmission through a thin fused silica plate heated to high temperature, similar to the approach taken by McLachlan [11]. The experimental setup is shown in Fig. 2. The 4.6 μm laser used throughout this study is based on a frequency-doubled, Q-switched, CO_2 laser operating at 9.2 μm (Coherent DEOS Mid-IR-2). The maximum second harmonic output power at 4.6 μm is 6 W (average) at a pulse repetition rate of 75 kHz and a pulse width of 22 ns. Despite the pulsed output, the 4.6 μm laser can be considered quasi-CW as will be shown later in the paper.

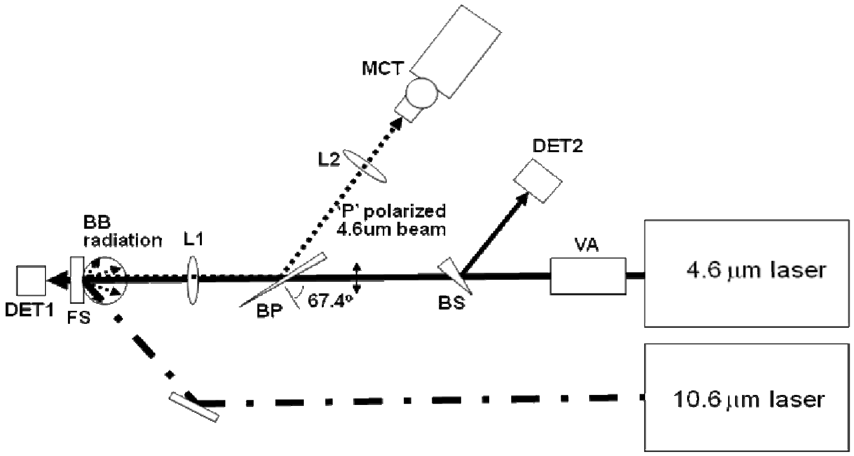

Figure 2: Experimental layout for absorption measurements and damage mitigation trials using 4.6 and 10.6 μm lasers. The Solid (dot-dashed) line shows the beam path for the 4.6 μm (10.6 μm) laser. The optical components are denoted by the following symbols: VA - variable attenuator, BS - wedged plate used for sampling incident 4.6 μm light, BP - wedged plate oriented at Brewster angle for separating 4.6 μm laser light from the black body radiation emitted from sample surface, L1/L2 - ZnSe lenses, FS - fuse silica sample, DET1/DET2 - MCT detectors coupled with integrating spheres, and MCT is the IR sensitive thermal camera.

The absorption coefficient measurement was made using a 1" diameter, 120±1 μm thick, plane-parallel fused silica plate made of Corning 7980 glass. The 4.6 μm laser beam is focused to a 1/e beam radius of 112 μm with a Rayleigh range of 17 mm at the fused silica plate and attenuated to ~180 mW to minimize 4.6 μm laser-heating of the plate. To vary sample temperature, a separate 10.6 μm laser (Synrad firestar V20) is introduced off-axis. The 10.6 μm laser heating beam, with a 2.8 mm horizontal and 1.7 mm vertical 1/e beam radius, is over-sized relative to the incident 4.6 μm laser beam to ensure that the radial and axial temperature profiles in the thin silica plate are uniform within the 4.6 μm illuminated region. With 4W of 10.6 μm laser power irradiating the plate, the temperature of the thin plate could be raised up to 2300 K, as verified *in-situ* using an infrared radiometry setup described elsewhere [12]. The transmission of 4.6 μm light through the fused silica plate was measured using the thermo-electrically cooled Mercury Cadmium Telluride (MCT) detectors (VIGO PVMI-2TE) that were attached to integrating spheres with infrared diffusive gold coatings (LabSphere LPM-020-IG). Referring to Fig. 2, DET1 was used to measure the transmitted 4.6 μm power, while DET2 monitored the incident

4.6 μm power. Care was taken to ensure that the detector was operating within its linear range and that no stray 10.6 μm laser light fell on either DET1 or DET2. The thermal emission from the heated silica plate was found to be negligible compared to the 4.6 μm laser light levels.

Figure 3a) shows the measured 4.6 μm laser transmission as a function of temperature. As shown, the transmission decreased from ~90% to ~60% as the fused silica plate temperature was increased from room temperature to 2300 K. Taking into account multiple reflections in a plane-parallel plate with internal loss [13], the extinction coefficients κ at the different temperatures were extracted from the transmission data and plotted in Fig. 3b). The derived extinction coefficient varies in a linear fashion from 0.0003±0.00005 at 300 K to 0.0013±0.00005 at 2000 K. A linear least squares fit yields a temperature dependent extinction coefficient of $\kappa(T) = 7.02\times10^{-5}+6.39\times10^{-7}T$, where T is in Kelvin. The measured room temperature extinction coefficient of 0.0003±0.00005 is in excellent agreement with reported literature value [9].

In Fig. 3c), the absorption coefficient α and absorption length α^{-1} calculated from the measured extinction coefficients as $\alpha = 4\pi\kappa/\lambda$ are plotted against temperature. The increase in absorption coefficient and the corresponding decrease in absorption length at elevated temperatures are consistent with what has been observed at 10.6 μm [11]. The magnitudes of the absorption coefficient and absorption lengths between the two wavelengths over the same temperature range, however, are quite different. Whereas in the 10.6 μm case, α (α^{-1}) varies from 250 cm^{-1} (40 μm) at 300 K to 2500 cm^{-1} (4 μm) at 2000 K, α (α^{-1}) at 4.6 μm changes from 7.2 cm^{-1} (1397 μm) to 36.8 cm^{-1} (271 μm) over the same temperature range. It is this ≥35× lower absorption coefficient at 4.6 μm relative to that at 10.6 μm that leads to a more penetrating temperature profile into fused silica with 4.6 μm laser-heating, and hence greater potential for sub-surface damage mitigation. The large variation in absorption length over temperature at 4.6 μm, however, suggests that it will be important to consider the form of *α(T)* when calculating temperature distribution, as we will see in the next section.

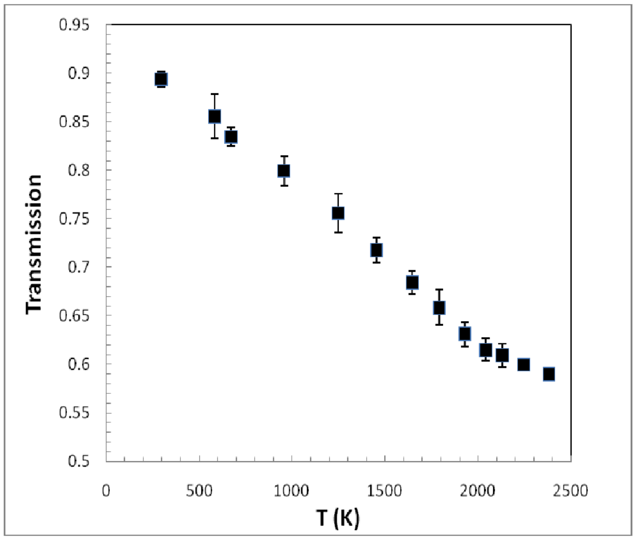

(a)

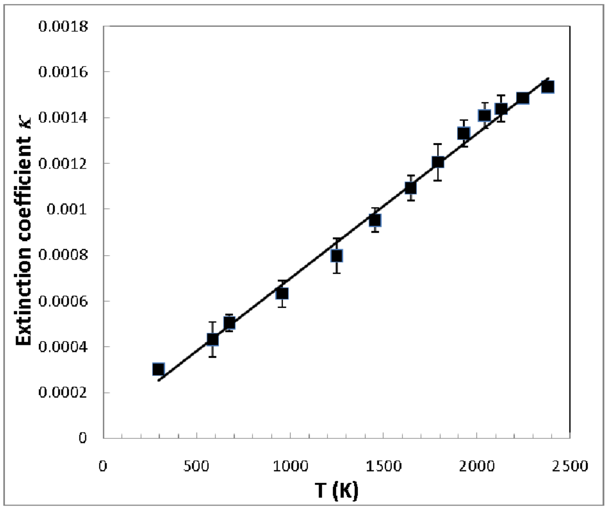

(b)

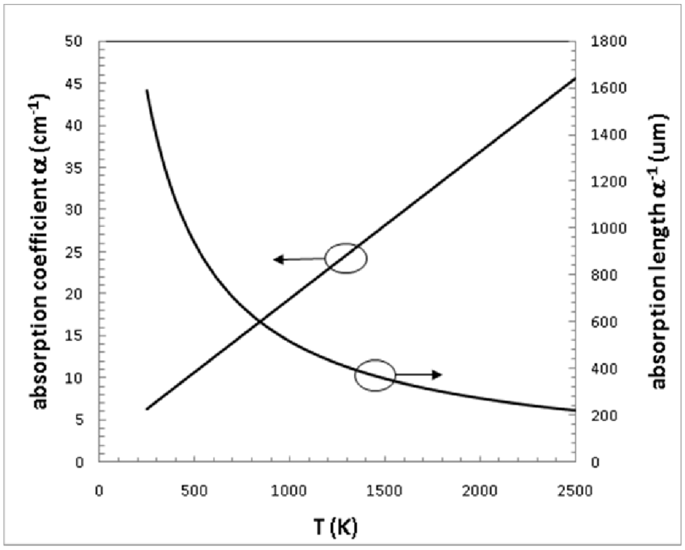

c)

Figure 3: Results from the measurement of $\alpha(T)$ at 4.6 μm showing a) the measured 4.6 μm transmission through thin fused silica plate, b) the extracted extinction coefficient κ based on the measured transmission with a linear least square fit, and c) the calculated fused silica α and α^{-1} at 4.6 μm as a function of temperature. The error bars In a) and b) represent one standard deviation variance from four measurements.

B. Solution to the 4.6 μm laser-driven heat flow equation using finite difference methods

To calculate the temperature distribution inside laser-heated fused silica under an axisymmetric geometry, we must solve the 2D heat flow equation [14],

$$\rho C_p \frac{\partial T}{\partial t} - \nabla(k\nabla T) = Q,$$

where ρ is the density, C_p is the specific heat, k is the thermal conductivity, and Q is the heat source term. In the case of volumetric heating with a Gaussian laser beam, the heat term is expressed as $Q(r,z) = (\alpha I)\exp(-\alpha z)\exp[-(r/a)^2]$, where the absorbed laser irradiance $I = (1-R)P/\pi a^2$ is a function of the wavelength-dependent silica reflectivity R, the incident laser power P, and the 1/e beam radius *a.* In the expression for *Q*, *r* and *z* are the usual radial and axial coordinates. For fused silica heated by a CW 10.6 μm laser, where the laser energy is mainly absorbed at the surface, it has been found that the temperature distribution can be adequately determined by treating the material parameters α, *k* and C_p as constants [15]. With these approximations, a simplified closed-form solution to the heat equation can be obtained [16]. Indeed, since the heating can be considered quasi-CW for the 4.6 μm case, the thermal parameters *k* and C_p can still be approximated as constants. However, due to the large variation in α over the temperature range of interest, and the fact that α^{-1} is no longer small compared to *a*, the temperature dependence of absorption, $\alpha(T)$, must be taken into account in solving the heat equation. As a consequence, a closed-form analytical solution to the heat flow equation does not exist and, accordingly, numerical methods must be sought. Following the work of Mansuripur *et al.* on non-uniform multilayer laser heating [17], we implement a finite difference scheme, and solve the heat equation assuming an axisymmetric geometry. We assume insulating boundary conditions, i.e. no heat loss mechanisms due to convective or evaporative cooling. Additionally, since the bulk heat transport is dominated by conduction, radiation loss is also ignored [12, 18].

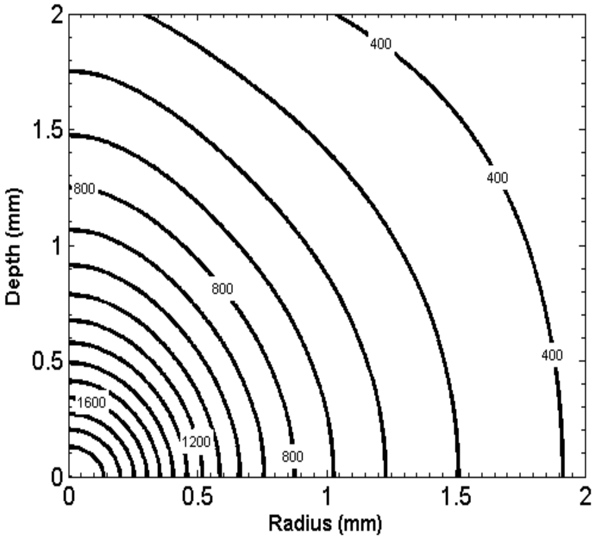

a)

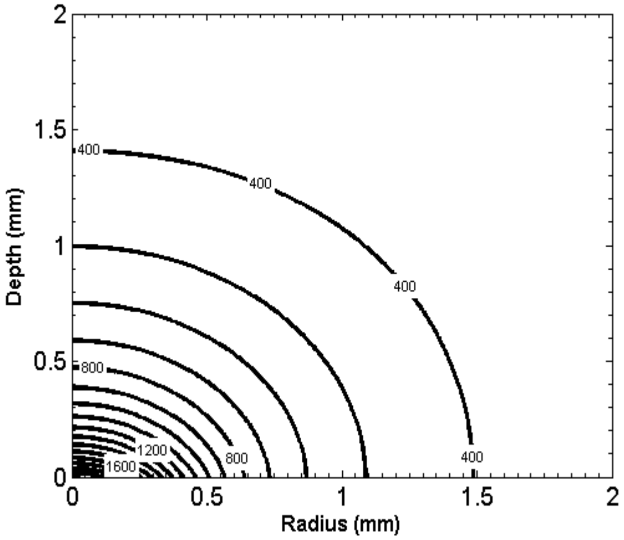

b)

Figure 4: Contour plots of the temperature distribution in fused silica at t= 10 seconds for a) 4.6 μm and b) 10.6 μm laser heating with 354 μm 1/e beam radius at power levels P=7.6W (4.6 μm) and P=5.2W (10.6 μm).

Figure 4 displays contour plots of the calculated temperature distribution inside fused silica at the end of a 10 second long exposure when heated with either a 4.6 μm (Fig. 4a) or a 10.6 μm laser (Fig. 4b). For these calculations, we used a=354μm in both cases, but with different power levels chosen for each laser: P=7.6 W for 4.6 μm laser and P=5.2 W for 10.6 μm laser. These power levels were chosen so as to achieve a peak surface temperature of ~2000 K in both cases. We note that the 2.4W additional power required for the 4.6 μm laser is a consequence of the decreased absorption of 4.6 μm laser light relative to that of the 10.6 μm laser. In Fig. 4, the contour lines are spaced apart by 100 K and the lowest temperature contour line in both plots is at 400 K. As evident from the plots, the contour lines in the 4.6 μm case are roughly circular and evenly spaced, consistent with a relatively deep heat penetration and shallow temperature gradient. This is in contrast to the 10.6 μm case, where the contour lines have a more asymmetric 'pancake' shaped distribution and are much more closely-spaced together, suggesting shallower heat penetration and steeper axial temperature gradients. The large heat-affected zone resulting from 4.6 μm laser-heating suggests that it will be more efficient at repairing deep surface fractures.

Figure 5a) shows the calculated radial surface temperature profiles at t=10s for the two laser cases. Consistent with the contour plots of Fig. 4, the 4.6 μm radial temperature profile is wider than that associated with 10.6 μm heating, resulting in lower radial temperature gradient for the same peak temperature. Within the first few hundred microns from beam center, however, the radial temperature profiles are quite similar for the two cases. In contrast, the difference between the axial temperature profiles at r=0 for the two lasers is more dramatic, as shown in Fig. 5b). For example, in the 4.6 μm case, the on-axis temperature rises to 1700 K at a depth of 280 μm below surface after 10 seconds, while the same is true at only 70 μm below surface for the 10.6 μm case. Not only is the heat penetration depth different, but the shape of the axial temperature distribution is also quite distinct between the two cases. Whereas in the 10.6 μm case, the axial temperature distribution has a very steep fall-off near the surface with an axial temperature gradient of -4.5 K/μm, the axial temperature gradient in the 4.6 μm case is only -0.3 K/μm at the surface and deviates less than 100 K over a depth of ~130 μm from the surface. Over the same 130 μm depth range, the 10.6 μm laser-heated silica drops by more than 500 K, implying a highly non-uniform thermal treatment over a depth range that is comparable to the expected UV laser-induced damage depths in silica [1, 19].

Figure 5c) shows the surface temperature at beam center (r=0, z=0) as a function of time. As with comparison of spatial temperature profiles (Fig. 5a and 5b), the temporal behavior of the two cases can be easily distinguished. Due to the reduced temperature gradient, and hence lower thermal conduction rate, it takes longer for the 4.6 μm laser case to reach a steady state temperature relative to the 10.6 μm laser case. For the calculation shown in Fig. 5c), the peak surface temperature does not reach 90% of steady state value until 1.69 seconds after laser turn-on for the 4.6 μm case, while it only took 0.7 seconds in the case of 10.6 μm laser. To heat fused silica to a desired steady state surface temperature using the 4.6 μm laser, therefore, would require higher power and longer time relative to heating to the same conditions using a 10.6 μm laser. The heat-affected volume and heat penetration depth, however, will be substantially larger in the 4.6 μm case.

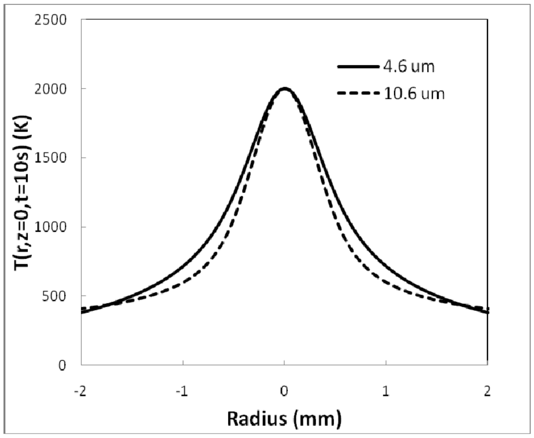

a)

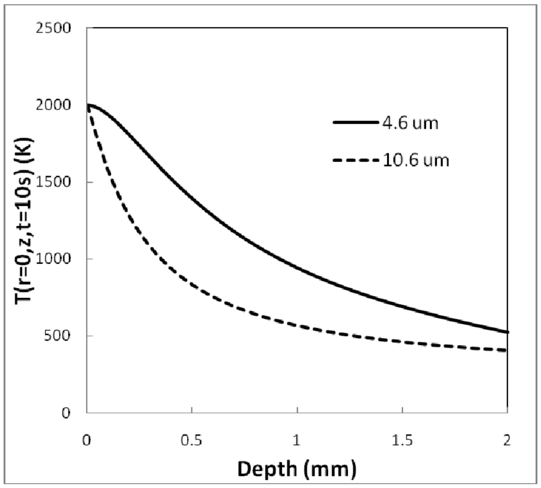

b)

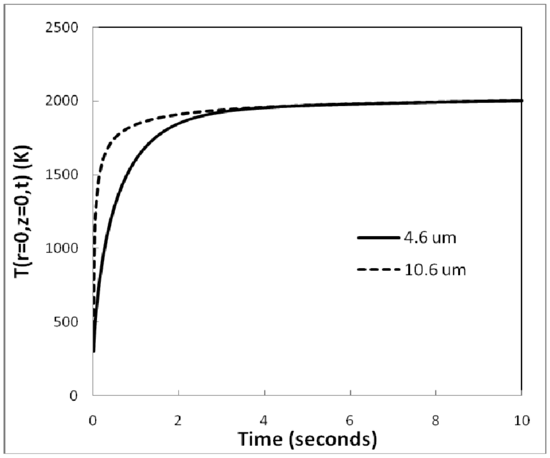

c)

Figure 5: Comparison of the calculated spatial and temporal temperature profiles of laser-heated fused silica using a 4.6 μm laser (solid) versus that using a 10.6 μm laser (dashed). a) Radial temperature profile comparison at z=0 and t=10s, b) axial temperature profile comparison at r=0 and t=10s, and c) temporal temperature profile comparison at r=z=0.

To compare our numerical model predictions with measurements, surface temperatures under different 4.6 μm laser irradiation conditions were measured *in-situ* using infrared radiometry [15]. The experimental setup for these measurements is the same as depicted in Fig. 2. The sample used for these measurements was a polished 2" diameter, 10 mm thick fused silica substrate made of Corning 7980 glass. The 4.6 μm laser power was varied by using a variable attenuator while holding all other parameters the same. Different beam radii were obtained at the sample by varying the distance between the final focusing lens and the sample, and the laser exposure was fixed at 10 seconds. Figure 6 shows the measured peak surface temperature at beam center, just before turn off of the 10 seconds long laser pulse, plotted as a function of incident laser power for 1/e beam radius of 140 μm, 216 μm and 332 μm. In all cases, the peak surface temperature is seen to rise up in a nonlinear fashion as the power is increased. This is in sharp contrast with the 10.6 μm laser heating case, where the temperature rise is found to be linear up to ~2800 K [15]. The good agreement between the measured data and the model indicates that the nonlinear temperature rise in the 4.6 μm case can be well-described using the measured temperature-dependent $\alpha(T)$: as temperature increases, fused silica absorption length shortens which in turn leads to an increased heat deposition close to the surface and hence to an accelerated rise in peak surface temperature. The nonlinear temperature rise versus power also implies that the heating of fused silica using a 4.6 μm laser is more sensitive to power fluctuations [16]. Therefore, a more stringent power control might be required for the 4.6 μm laser over that of the 10.6 μm laser to obtain consistent laser heating results. The nonlinear temperature rise continues until the peak surface temperature reaches ~2100 K. At this point, additional nonlinearities developed, the cause of which is not understood at present.

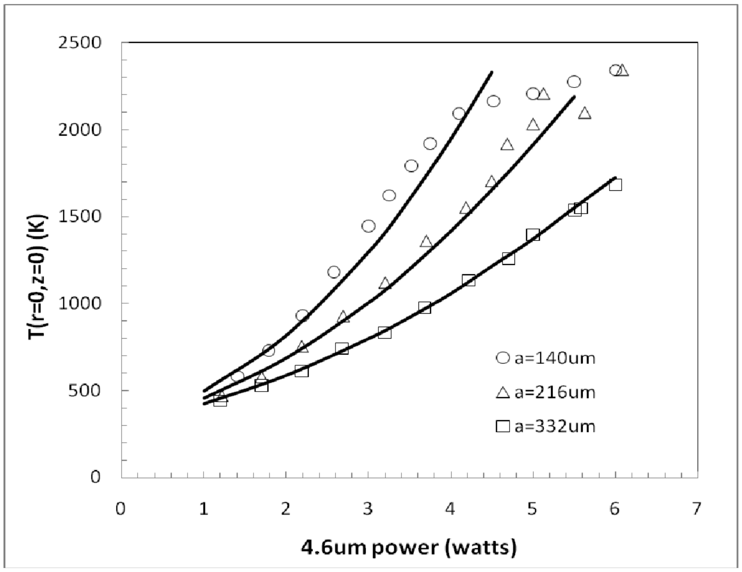

Figure 6: Measured (symbols) and calculated (lines) peak surface temperature at the end of 10 second exposure versus incident 4.6 μm laser power for beam radius of 140, 216 and 332 μm

In addition to measuring the steady-state peak surface temperatures, the surface temperature profiles of fused silica heated with the 4.6 μm laser was also measured and compared with prediction. Figure 7 shows the measured and calculated radial temperature profiles for a 4.6 μm laser power of 4.6

W, beam radius of 216 μm, and at 10 seconds after laser turn-on. As shown, there is excellent agreement between measurement and calculation.

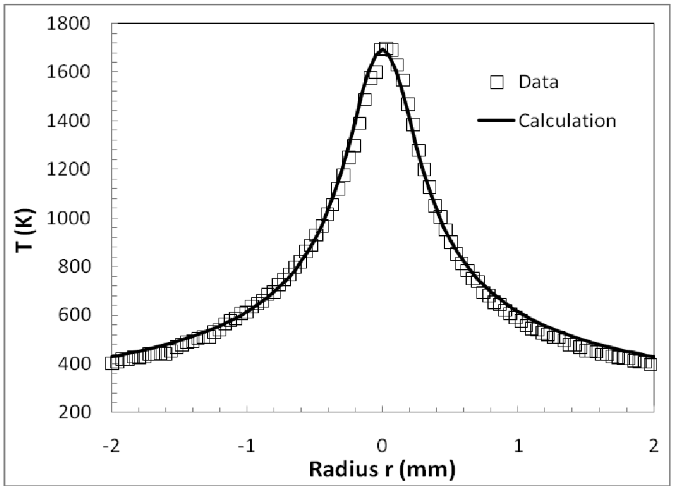

Figure 7: Comparison of the measured and predicted radial surface temperature profiles for 4.6 μm laser-heated fused silica, 10 seconds after laser turn-on. The laser power was 4.6 W and the 1/e beam radius was 216 μm.

To confirm that our model also captures the surface temperature dynamics, peak surface temperature temporal profiles were also recorded by setting the thermal camera to a video capture frame rate of 32.8 frames per second, with a frame averaging time of 200 μs. The result of one such measurement is shown in Fig. 8, where the peak surface temperatures at beam center from each of the 300 frames recorded are plotted against time. The laser parameters used were P=4.6W, a=216 μm, and the laser was turned on at t=0 and turned off at t=10 seconds. Overlaid with the recorded temporal data is the calculated temperature evolution assuming a continuous-wave flat-top pulse lasting 10s. The excellent agreement between the measured data and the model prediction confirms that the 4.6 μm laser is indeed behaving like a CW laser source, and further validates our finite difference numerical model.

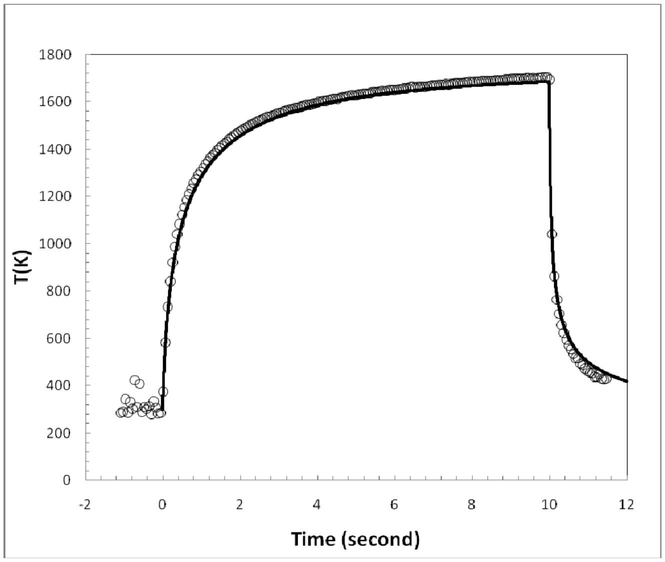

Figure 8: Measured and predicted peak surface temperature as a function of time during a 4.6 W exposure of 4.6 μm light with a 1/e beam radius of 216 μm. Each temperature data point is averaged over 200 μs.

3. Characterization of the heat affected zone using confocal Raman microscopy

In this section, we examine in further detail the sub-surface temperature changes in bulk fused silica caused by laser-heating. Since our infrared radiometry is limited to measuring surface temperatures only, an alternate technique is needed to probe heating inside the bulk. One method that can be used to characterize the heat-affected zone in laser-heated glasses is to measure the spatially-dependent *fictive temperature* changes associated with glass thermal history [20]. The fictive temperature, T_f, is defined as the thermodynamic temperature (T) at which the glass structure would be in equilibrium. When glass is subjected to thermal cycle, the glass structure attempts to attain thermal equilibrium at the prevailing thermodynamic temperature, limited by the finite glass structural relaxation time. Because the structural relaxation time τ decreases exponentially with increasing temperature, glass relaxation is rapid at high temperature and T_f tends to track the instantaneous thermodynamic temperature at high T. However, as glass cools below the glass transition point ($T=T_g$), relaxation proceeds more slowly, and the glass structure is eventually frozen into a non-equilibrium state that persists down to room temperature. Thus, the faster the glass cools from high temperature, the less chance there is for the glass structure to relax before it is frozen-in and the closer the final T_f will be to the peak thermodynamic temperature immediately prior to cool down. The rapid cooling associated with an abrupt laser turn-off, therefore, offers a 'snapshot' of the thermodynamic temperature at the instant of laser turn-off to be taken in the form of T_f. By spatially mapping the final T_f following a laser exposure, one can then deduce the extent of heat penetration due to laser-heating.

To measure T_f, we used confocal Raman microscopy because of its high 3D spatial resolution and non-destructive nature. A detailed description of our Raman setup and fictive temperature mapping will be published elsewhere [21]. Briefly, our confocal Raman microscope uses a 532 nm diode-pumped solid state laser as the pump source, with a confocal setup that limits the sampled region to ~ 2 μm radially and 5 μm axially. Raman spectra were collected from discrete locations within the bulk, along the center-line of the laser-heated regions. To deduce fictive temperature from the Raman spectrum, the ratio of the D_2 defect band area relative to ω_1 band intensity was measured and interpreted using an Arrhenius relationship [22], assuming a D_2 activation energy of 0.4 eV, and a background T_f level taken from an oven-annealed sample with no laser treatment.

Figure 9 presents the results of fictive temperature measurements collected along r=0, $T_f(z)$, on samples exposed to 4.6 and 10.6 μm laser sources. The 4.6 μm laser-irradiated sites were created with P=6 W, a= 300 μm, and exposure times of 10s and 300s; while for the 10.6 μm laser, P=5.8 W, a=339 μm, and the same exposure times were used. These laser parameters were chosen to yield similar (~2000K) peak surface temperatures and to minimize material loss due to evaporation. In all cases, $T_f(z)$ peaks at the surface and follows a roughly sigmoidal depth dependence from $T_{f,max}$ to $T_{f,min}$~T_g. For the shorter exposure times, $T_{f,max}$ was roughly 1900K for the 10.6 μm case, and 1800 K for 4.6 μm, indicating the longer relative thermal diffusion time for 4.6 um laser-heating. At longer exposure times, however, the peak fictive temperature for each cases was nearly identical, $T_{f,max}$~2000 K. For either exposure times, the extent of the heat affected regions, where T_f is elevated above T_g, is greater for the 4.6 μm case versus the 10.6 μm case. Specifically, the 4.6 μm laser heat-affected depths, inferred from the measured $T_f(z)$, are found to be 255 and 394 μm for the 10 and 300 second exposures respectively, or roughly twice as deep as the heat affected depths for the equivalent 10.6 μm cases (131 and 204 μm respectively). In addition, it should be noted that the relative axial gradient in $T_f(z)$ is less under 4.6 μm laser-heating, consistent with the lower axial temperature gradients calculated in the previous section.

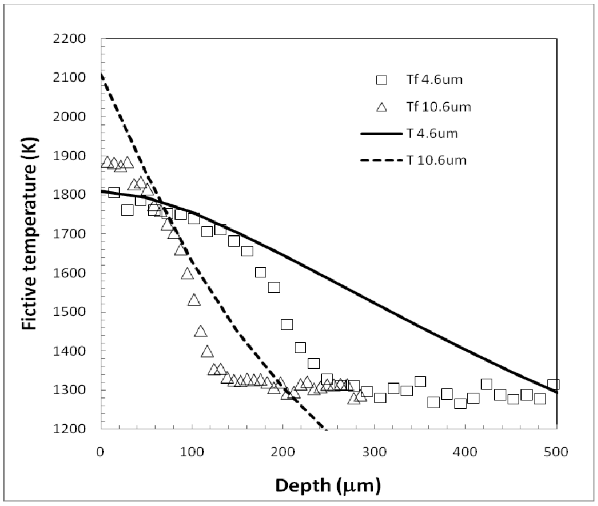

a)

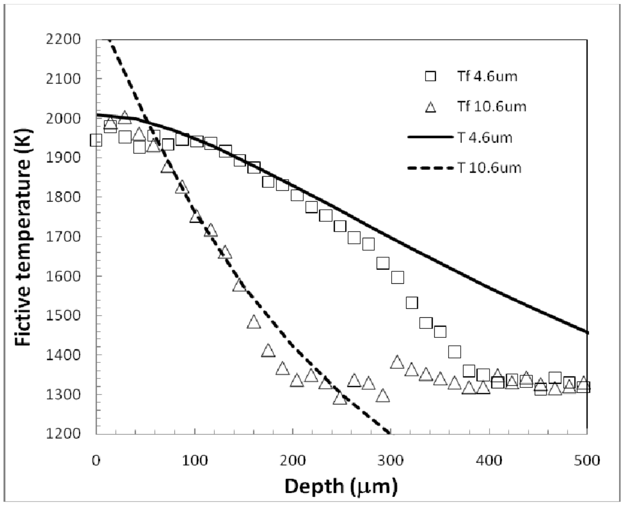

b)

Figure 9: Fictive temperature profiles measured along r=0 as a function of depth in fused silica for 4.6 μm (⍰) and 10.6 μm (Δ) irradiated sites. The sites were exposed for a total of a) 10 s and b) 300 s with fluences that were chosen to limit surface temperatures to <2000 K. Lines are the calculated thermodynamic temperature profiles just prior to laser turn-off.

For direct comparison of the fictive and thermodynamic temperatures T just before laser quench ($t=t_{off}$), we plot along with $T_f(z)$ in Fig. 9 calculated values for $T(r=0,z, t=t_{off})$ using our finite difference model. As shown, T_f tracks T closely near the surface where temperatures are far above T_g (i.e. 1700K<T<2000K), but deviates from T farther into the bulk as temperatures approach T_g. As discussed previously, the close tracking near the surface and subsequent divergence of T_f relative to T in the bulk is indicative of the magnitude of the structural relaxation time constant τ at the various depths. The degree of relaxation thus revealed can be used to qualitatively assess the likelihood of cracking healing in the bulk. For example, near the surface where T_f tracks T, the low viscosities leading to the shorter relaxation time should also promote crack closure. Conversely, at depths beyond a few hundred microns where T<1700K, the deviation of T_f and T implies that relaxation times are much longer at these depths and hence the viscosity is too high for crack healing to occur. These observations suggest that one can define the depth where the fictive temperature starts to depart from the thermodynamic temperature (i.e. T=1700 K) as an effective crack healing depth, z_{eff}, within which significant structural change and crack healing can occur over reasonable experimental time scales. This assumption can be checked by estimating the time that is required for a crack of width w to close up due to capillary-driven viscous flow as $\tau_c \sim \eta w/\pi\sigma$ [23], where η is the viscosity and σ is the surface tension. At 1700K, the viscosity of silica is 3.9×10^9 poise and the surface tension is 300 dynes/cm [24-25], which yields crack closure times τ_c in the range of ~40-400s for length scales w ranging from 0.1 to 1μm. Thus, using this simple approximation, the healing of micron-sized cracks along fractures extending to depths where T>1700K should occur over several minutes of laser-heating.

4. Figure of merit for deep crack healing in silica

Using the effective crack healing depth z_{eff} defined above, combined with a requirement to minimize mass loss by limiting surface temperature to 2000K maximum (i.e. $T(z=0) \leq 2000$K), we can define a Figure Of Merit (FOM) that quantifies the efficiency of crack healing as $FOM = z_{eff}/P_o$, where P_o is the minimum incident laser power required to achieve a peak surface temperature of 2000 K. Since surface heating dominates for the 10.6 μm case ($a >> \alpha^{-1}$), the FOM defined above can be readily calculated using an analytic expression for the steady-state axial temperature [16]:

$$T_z(P,a,z) = \frac{(1-R)P}{2ak\sqrt{\pi}}(1-Erf(z/a))Exp((z/a)^2) + T_0, \qquad (2)$$

where T_0 is the ambient room temperature. From Eq. (2), it can be seen that to achieve a peak surface temperature T_p of 2000 K would require a normalized power of $\frac{P_o}{a} = \frac{2k\sqrt{\pi}}{(1-R)}(T_p - T_0)$, which equals 142 W/cm assuming $1-R$ = 0.85 and k=0.02 W cm^{-1} K^{-1} for fused silica. Applying this ratio to Eq. (2), we can then solve for the normalized effective crack healing depth z_{eff}/a, which yields a constant value of 0.182. The FOM for 10.6 μm laser-heating is therefore found to be a constant: *FOM (10.6 μm)* = $0.182/142\times10^4$ = 12.8 μm/W. Equivalently, to achieve a depth z_{eff} of z_0 μm using a 10.6 μm laser would require an incident power of $P_o=z_0/12.8$ W with a beam radius of $a= z_0/0.182$ μm. Similar calculations were done for the 4.6 μm laser-heating case by applying the numerical temperature distribution model described in Sec. 2. Figure 10a) shows the calculated effective crack healing depth z_{eff} versus incident laser power for the two laser wavelengths, while Fig. 10b) plots the corresponding *FOM* against z_{eff}. It is evident from the figures that, up to a depth of 500 μm considered here, it is more efficient to heal sub-surface cracks by laser-heating at 4.6 μm rather than at 10.6 μm, particularly for small z_{eff}. For example, to achieve a z_{eff} of 200 μm using a 4.6 μm laser would only require a power of 4.1 W focused to a 1/e beam radius of a=100 μm. In contrast, to achieve the same z_{eff} using a 10.6 μm laser would require as much as 16 W of power spread out over a radius of a= 1100 μm. The efficient heat penetration using 4.6 μm laser in this case is reflected in the much higher *FOM*(4.6μm) of 48.7 μm/W, which is 3.8 times the 10.6 μm laser FOM. The advantage of 4.6 μm laser-heating relative to 10.6 μm, however, is diminished as z_{eff} is increased. As shown in Fig. 10a), z_{eff} rises up sub-linearly as a function of incident 4.6 μm power, resulting in a corresponding decline in *FOM* until *FOM*(4.6μm) is predicted to approach *FOM*(10.6μm) for z_{eff} >>500 μm. The decline of 4.6 μm *FOM* can be attributed to the increase in beam radius a that is required to achieve deeper z_{eff} such that in the limit of large z_{eff} the surface heating condition, $a>>\alpha^{-1}$, is approached and any further increase in 4.6μm power produces a linear increase in z_{eff} as in the 10.6 μm case. Nonetheless, for crack healing to depths of at least 500 μm, the laser heating will be more efficient and the treatment can remain well-localized using a 4.6 μm laser as compared to a 10.6 μm laser.

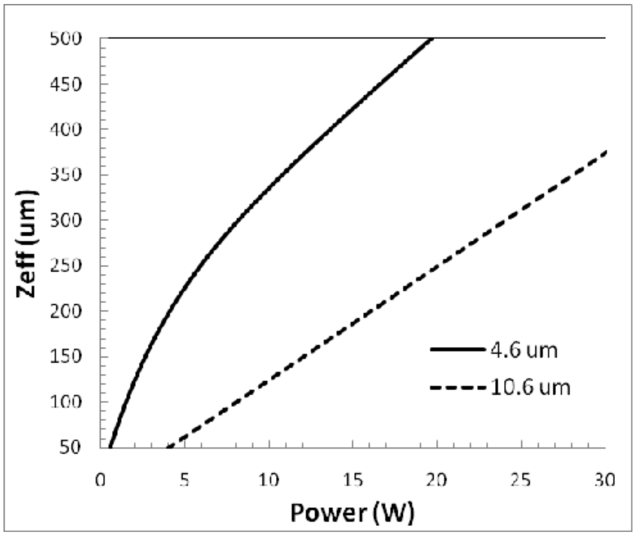

a)

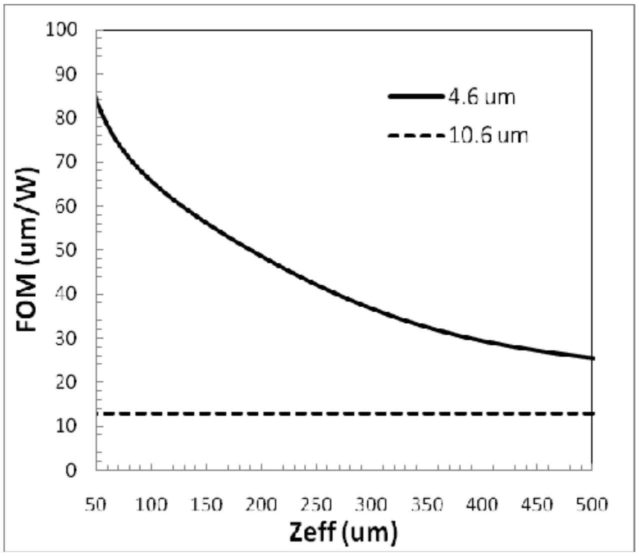

b)

Figure 10: a) The calculated effective crack healing depth z_{eff} as a function of laser power for both 4.6 and 10.6 μm cases, and b) a comparison of the Figure of Merit (FOM) for each laser, as defined in the text, plotted against z_{eff} .

5. Demonstration of damage tracks repaired using 4.6 μm laser

To demonstrate healing of deep cracks while minimizing ablation, damaged tracks were created in fused silica and subsequently heated with 4.6 μm laser to peak surface temperature of 2000 K. These damaged tracks were created in 40mm×5mm×9mm slabs of fused silica material that are polished on all sides to allow for inspection of the damage tracks from the sides. Damage was initiated by focusing the 355 nm output from a Q-switched Nd:YAG laser on the exit surface of the slabs. Typically, ~5 mJ of pulse energy focused into a 100 μm spot is sufficient to initiate damage. The initiated surface damage is then extended into the bulk through multiple laser shots. Damage tracks with lengths up to 300 μm and with transverse dimension of ~150 μm are produced in this manner.

Figure 11a) is a microscope image of a damage track when viewed from the side. The damage created is characterized by a surface crater with a central crack core that extends 225 μm into the bulk, and fine hair-line cracks that extend laterally from the central damage core. The damage track shown in Fig. 11a) was subsequently subjected to 4.6 μm laser-heating with a 1/e beam radius of 281 μm. To minimize formation of bubbles as noted by Guss previously [10], the 4.6 μm power was slowly raised in five equal time steps lasting 60 s each following the power sequence of 2.4W, 3.5W, 4.7W, 5.6W and 6W. During heating, the damage track was imaged from the polished side to monitor the progression of crack healing using a camera. At the lowest two power levels, as the silica was slowly being heated up, no discernible changes to the damage track occurred. At the onset of 4.7W of power, hair-line cracks near the central damage core just below the surface crack were observed to coalesce and slowly disappear. This was followed by a rapid erasure of central crack core when the power was next raised to 5.6 W, accompanied by a smoothing of the surface crater. Finally, as the power was raised to 6 W, the remaining cracks in the bulk were seen to disappear, followed by a leveling of the surface crater into a shallow pit, as the viscosity decreased enough for surface tension-driven flow to fill in the surface crater.

At the end of 300 s irradiation, the original damage track was completely healed, leaving a smooth rimless parabolic-shaped crater that is 3.6 μm deep and 340 μm in diameter at the surface as shown in Fig. 11b) and c).

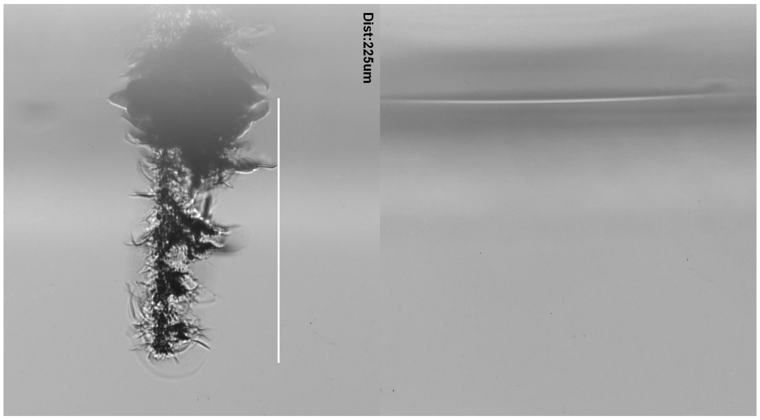

Fig. 11a) & b)

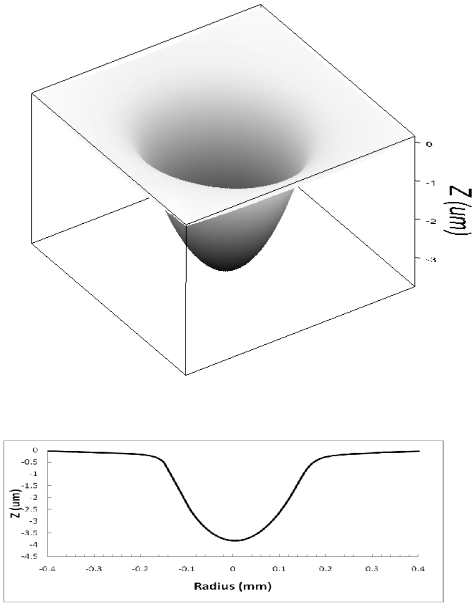

c)

Figure 11: Side view of damage track before a) and after b) irradiation with a 4.6 μm laser exposure. The damage track extends 225 μm below surface as indicated by the white bar. After laser-heating, the cracks are entirely erased leaving a shallow crater as shown in c).

To compare with a 10.6 μm laser-heating treatment, a similar set of damage tracks were created and exposed to a 10.6 μm laser with P= 4.8 W and a=354 μm so as to limit maximum surface temperature to 2000 K. Figure 12a) shows a side-view image of a damage track prior to 10.6 μm laser heating. As shown, even after 300 seconds of heating at 4.8 W, the maximum crack healing extended to only 40 μm below surface as shown in Fig. 12b), in accord with the measurements and model predictions discussed in the previous sections.

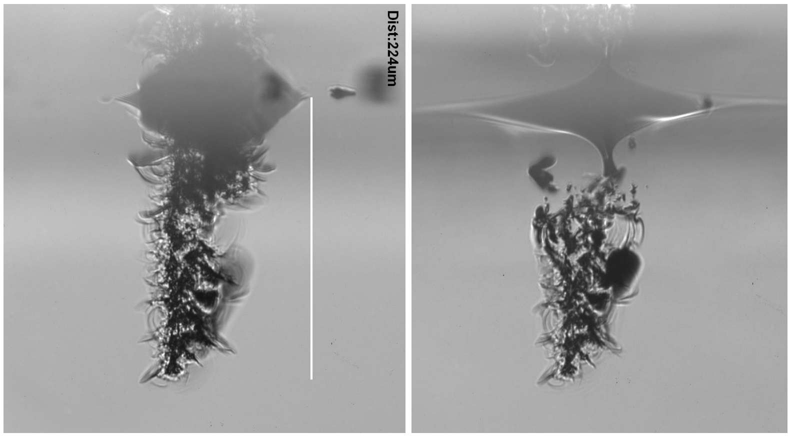

Figure 12: Side views of damage tracks before a) and after b) heating by 10.6 μm laser. Crack healing extended to only 40 μm below surface.

6. Conclusions

A study comparing the use of mid- versus far-IR lasers to thermally mitigate surface damage in fused silica has been presented. Direct measurement of the temperature-dependent absorption coefficient of fused silica at 4.6 μm revealed that α is a factor of 35 times lower at 4.6 μm versus 10.6 μm at room temperature, resulting in deeper heat penetration depths and shallower temperature gradients. Solving the heat conduction equation numerically with the measured $\alpha(T)$, we find the inclusion of temperature dependent $\alpha(T)$ can explain the nonlinearity in peak surface temperature versus laser power observed in the 4.6 μm laser-heating case, in contrast with the linear relationship in the 10.6 μm case. Thermal model predictions were confirmed experimentally using infrared radiometry and confocal Raman microscopy, with the latter being used to establish an effective crack healing depth z_{eff} for damage mitigation. Based on z_{eff}, and imposing a minimum mass loss condition (i.e. $T(z=0) \leq 2000$ K), we propose a figure of merit (FOM) that quantifies damage mitigation efficiency as a function of laser parameters. It was found that, for damage sites with sub-surface cracks extending 500 μm below the surface, 4.6 μm laser-heating proved to be a more efficient and better-localized laser treatment. In support of these conclusions, we irradiated pulsed-laser-induced damage tracks with a 4.6 μm laser, limiting peak surface temperatures to 2000 K, and demonstrated the healing of sub-surface fractures to a depth of ~225 μm. In contrast, crack healing was limited to only ~40 μm in depth using a 10.6 μm laser under similar surface heating constraints. The potential for deep crack healing, combined with well-localized non-ablative heating, are key advantages of mid-IR laser-based damage mitigation versus that based on far-IR lasers at 10.6 μm.

The authors would like to acknowledge Dr. Michael Feit, Dr. James Stolken, Ryan Vignes, and Dr. Isaac Bass for stimulating discussions relating to numerical solution of the heat equation. We would also like to thank Dr. Paul Mak from Naval Research Laboratory for the generous loan of the 4.6 μm laser. This work performed under the auspices of the U.S. Department of Energy by Lawrence Livermore National Laboratory under contract DE-AC52-07NA27344.

Figure Captions

Figure 1: Room temperature absorption spectrum of fused silica reproduced from Ref. [9]. Note that the absorption coefficient at 4.6 μm is about two orders of magnitude lower than that at 10.6 μm.

Figure 2: Experimental layout for absorption measurements and damage mitigation trials using 4.6 and 10.6 μm lasers. The Solid (dot-dashed) line shows the beam path for the 4.6 μm (10.6 μm) laser. The optical components are denoted by the following symbols: VA - variable attenuator, BS - wedged plate used for sampling incident 4.6 μm light, BP - wedged plate oriented at Brewster angle for separating 4.6 μm laser light from the black body radiation emitted from sample surface, L1/L2 - ZnSe lenses, FS - fuse silica sample, DET1/DET2 - MCT detectors coupled with integrating spheres, and MCT is the IR sensitive thermal camera.

Figure 3: Results from the measurement of $\alpha(T)$ at 4.6 μm showing a) the measured 4.6 μm transmission through thin fused silica plate, b) the extracted extinction coefficient κ based on the measured transmission with a linear least square fit, and c) the calculated fused silica α and α^{-1} at 4.6 μm as a function of temperature. The error bars In a) and b) represent one standard deviation variance from four measurements.

Figure 4: Contour plots of the temperature distribution in fused silica at t= 10 seconds for a) 4.6 μm and b) 10.6 μm laser heating with 354 μm 1/e beam radius at power levels P=7.6W (4.6 μm) and P=5.2W (10.6 μm).

Figure 5: Comparison of the calculated spatial and temporal temperature profiles of laser-heated fused silica using a 4.6 μm laser (solid) versus that using a 10.6 μm laser (dashed). a) Radial temperature profile comparison at z=0 and t=10s, b) axial temperature profile comparison at r=0 and t=10s, and c) temporal temperature profile comparison at r=z=0.

Figure 6: Measured (symbols) and calculated (lines) peak surface temperature at the end of 10 second exposure versus incident 4.6 μm laser power for beam radius of 140, 216 and 332 μm.

Figure 7: Comparison of the measured and predicted radial surface temperature profiles for 4.6 μm laser-heated fused silica, 10 seconds after laser turn-on. The laser power was 4.6 W and the 1/e beam radius was 216 μm.

Figure 8: Measured and predicted peak surface temperature as a function of time during a 4.6 W exposure of 4.6 μm light with a 1/e beam radius of 216 μm. Each temperature data point is averaged over 200 μs.

Figure 9: Fictive temperature profiles measured along r=0 as a function of depth in fused silica for 4.6 μm (□) and 10.6 μm (Δ) irradiated sites. The sites were exposed for a total of a) 10 s and b) 300 s with fluences that were chosen to limit surface temperatures to <2000 K. Lines are the calculated thermodynamic temperature profiles just prior to laser turn-off.

Figure 10: a) The calculated effective crack healing depth z_{eff} as a function of laser power for both 4.6 and 10.6 μm cases, and b) a comparison of the Figure of Merit (FOM) for each laser, as defined in the text, plotted against z_{eff} .

Figure 11: Side view of damage track before a) and after b) irradiation with a 4.6 μm laser exposure. The damage track extends 225 μm below surface as indicated by the white bar. After laser-heating, the cracks are entirely erased leaving a shallow crater as shown in c).

Figure 12: Side views of damage tracks before a) and after b) heating by 10.6 μm laser. Crack healing extended to only 40 μm below surface.

Reference

1. M. A. Norton, L. W. Hrubesh, W. Zhouling, E. E. Donohue, M. D. Feit, M. R. Kozlowski, D. Milam, K. P. Neeb, W. A. Molander, A. M. Rubenchik, W. D. Sell, and P. Wegner, "Growth of laser initiated damage in fused silica at 351 nm," Proc. SPIE - Int. Soc. Opt. Eng. **4347**, 468-468 (2001).
2. L. W. Hrubesh, M. A. Norton, W. A. Molander, E. E. Donohue, S. M. Maricle, B. M. Penetrante, R. M. Brusasco, W. Grundler, J. A. Butler, J. W. Carr, R. M. Hill, L. J. Summers, M. D. Feit, A. Rubenchik, M. H. Key, P. J. Wegner, A. K. Burnham, L. A. Hackel, and M. R. Kozlowski, "Methods for mitigating surface damage growth in NIF final optics," Proc. SPIE - Int. Soc. Opt. Eng. **4679**, 23-33 (2002).
3. I. L. Bass, V. G. Draggoo, G. M. Guss, R. P. Hackel, and M. A. Norton, "Mitigation of laser damage growth in fused silica NIF optics with a galvanometer scanned CO_2 laser," High-Power Laser Ablation VI, Pts 1 and 2 **6261**, A2612-A2612 (2006).
4. I. L. Bass, G. M. Guss, and R. P. Hackel, "Mitigation of laser damage growth in fused silica with a galvanometer scanned CO_2 laser," Laser-Induced Damage in Optical Materials: 2005 **5991**, C9910-C9910 (2005).
5. R. M. Brusasco, B. M. Penetrante, J. A. Butler, and L. W. Hrubesh, "Localized CO_2 laser treatment for mitigation of 351 nm damage growth on fused silica," Laser-Induced Damage in Optical Materials: 2001 Proceedings **4679**, 40-47 (2002).
6. S. Palmier, L. Gallais, M. Commandre, P. Cormont, R. Courchinoux, L. Lamaignere, J. L. Rullier, and P. Legros, "Optimization of a laser mitigation process in damaged fused silica," Applied Surface Science **255**, 5532-5536 (2009).
7. M. J. Matthews, I. L. Bass, G. M. Guss, C. C. Widmayer, and F. L. Ravizza, "Downstream intensification effects associated with CO_2 laser mitigation of fused silica - art. no. 67200A," Laser-Induced Damage in Optical Materials: 2007 **6720**, 67200A67201-67200A67209 (2008).
8. E. Mendez, K. M. Nowak, H. J. Baker, F. J. Villarreal, and D. R. Hall, "Localized CO_2 laser damage repair of fused silica optics," Applied Optics **45**, 5358-5367 (2006).
9. R. Kitamura, L. Pilon, and M. Jonasz, "Optical constants of silica glass from extreme ultraviolet to far infrared at near room temperature," Appl. Opt. **46**, 8118-8133 (2007).
10. G. Guss, I. Bass, V. Draggoo, R. Hackel, S. Payne, M. Lancaster, and P. Mak, "Mitigation of growth of laser initiated surface damage in fused silica using a 4.6-micron wavelength laser," Proc. SPIE - Int. Soc. Opt. Eng. **6403**, 64030M-64031 (2006).
11. A. D. McLachlan and F. P. Meyer, "Temperature dependence of the extinction coefficient of fused-silica for CO_2-laser wavelengths," Applied Optics **26**, 1728-1731 (1987).
12. S. T. Yang, M. J. Matthews, and S. Elhadj, "Thermal transport in CO_2 laser irradiated fused silica: in situ measurements and analysis " Journal of Applied Physics **106**, 1031061-1031067 (2009).
13. O. S. Heavens, *Optical Properties of Thin Solid Films* (Dover Pub., 1965).
14. H. S. Carslaw and J. C. Jaeger, *Conduction of Heat in Solids,* 2nd ed. (Oxford University Press, 2000).
15. S. T. Yang, M. J. Manyalibo, S. Elhadj, V. G. Draggoo, and S. E. Bisson, "Thermal transport in CO_2 laser irradiated fused silica: *In situ* measurements and analysis," J. Appl. Phys. (2009).
16. M. v. Allmen and A. Blatter, *Laser-Beam Interactions with Materials,* 2nd ed., Springer Series in Materials Science (Springer, Berlin, 1995).

17. M. Mansuripur, G. A. N. Connell, and J. W. Goodman, "Laser-induced local heating of multilayers," Appl. Opt. **21**, 1106-1114 (1982).
18. S. Elhadj, M. J. Matthews, S. T. Yang, D. Cooke, J. S. Stolken, R. M. Vignes, V. G. Draggoo, and S. E. Bisson, "Determination of the intrinsic temperature dependent thermal conductivity from analysis of surface temperature of laser irradiated materials," Applied Physics Letters (accepted).
19. M. A. Norton, J. J. Adams, C. Wren Carr, E. E. Donohue, M. D. Feit, R. P. Hackel, W. G. Hollingsworth, J. A. Jarboe, M. J. Matthews, A. M. Rubenchik, and M. L. Spaeth, "Growth of laser damage in fused silica: diameter to depth ratio," Proc. SPIE - Int. Soc. Opt. Eng. **6720**, 67200H-67201(2007).
20. Z. Jian, J. Sullivan, J. Zayac, and T. D. Bennett, "Structural modification of silica glass by laser scanning," J. Appl. Phys. **95**, 5475-5482 (2004).
21. M. J. Matthews, R. M. Vignes, D. Cooke, S. T. Yang, and J. S. Stolken, "Analysis of micro-structural relaxation phenomena in laser-modified fused silica using confocal Raman microscopy," Applied Physics Letters (submitted).
22. A. E. Geissberger and F. L. Galeener, "Raman studies of vitreous SiO_2 versus fictive temperature," Physical Review B **28**, 3266-3271 (1983).
23. M. D. Feit and A. M. Rubenchik, "Mechanisms Of CO_2 laser mitigation of laser damage growth in fused silica," Laser-Induced Damage in Optical Materials: 2002 and 7th International Workshop on Laser Beam and Optics Characterization **4932**, 91-102 (2002).
24. R. H. Doremus, "Viscosity of silica," J. Appl. Phys. **92**, 7619-7629 (2002).
25. N. M. Parikh, "Effect of Atmosphere on Surface Tension of Glass," Journal of The American Ceramic Society **41**, 4 (1958).